IEEE Open Journal of
Ultrasonics, Ferroelectrics, and Frequency Control

Received 17 February 2022; revised 30 March 2022; accepted 29 April 2022.
Date of publication 4 May 2022; date of current version 20 May 2022.

Digital Object Identifier 10.1109/OJUFFC.2022.3172665

Physical Cause and Impact of Negative Capacitance Effect in Ferroelectric P(VDF-TrFE) Gate Stack and Its Application to Landau Transistor

KHOIROM JOHNSON SINGH (Graduate Student Member, IEEE), NITANSHU CHAUHAN, (Member, IEEE), ANAND BULUSU, (Member, IEEE), AND SUDEB DASGUPTA, (Member, IEEE)

Microelectronics and VLSI Group, Department of Electronics and Communication Engineering, Indian Institute of Technology Roorkee, Roorkee 247667, India

CORRESPONDING AUTHORS: KHOIROM JOHNSON SINGH; SUDEB DASGUPTA (ksingh5@ec.iitr.ac.in; sudeb.dasgupta@ece.iitr.ac.in)

This work was supported by the Ministry of Science and Technology, Department of Science and Technology, Government of India, under the Innovation in Science Pursuit for Inspired Research (INSPIRE) Fellowship, under Grant DST/INSPIRE Fellowship/IF180710.

ABSTRACT A novel approach to overcome Boltzmann's tyranny is to exploit the negative capacitance (NC) effect found naturally in many ferroelectric (FE) materials. We apply a set of coupled equations based on electrostatics, Kirchoff's law, and a well-calibrated Ginzburg-Landau-Khalatnikov technology computer-aided design (TCAD) model to simulate an organic FE poly(vinylidene fluoride-*co*-trifluoroethylene) [P(VDF-TrFE)]-based resistor metal-FE-metal (***R***-MFM) series circuit and a Landau transistor (LT) exhibiting sub-60 mV/decade subthreshold swing (*SS*). TCAD simulation parameters for P(VDF-TrFE) are derived from the reported experimental polarization versus voltage characteristics using Landau theory. Unlike oxide FEs, the P(VDF-TrFE)-based ***R***-MFM series circuit can exploit the NC effect at a lower supply voltage ($\boldsymbol{V_G}$) of $\pm$0.5 V with little energy dissipation of $\sim$2.7 fJ through ***R***. Our simulation results show an 84.89% reduction in the P(VDF-TrFE)'s coercivity concerning the oxide FE. We show that the underlying mechanism of the NC effect is directly related to FE polarization (FE-$\boldsymbol{P}$) switching. The NC effect occurs only when the FE-$\boldsymbol{P}$ is in the negative curvature of the P(VDF-TrFE)'s free energy landscape. The NC effect is explored in terms of $\boldsymbol{V_G}$, FE thickness, domain variations, ***R***, and dipole switching resistivity. The influence of ***R*** variation on the NC time ($\boldsymbol{\delta t}$) is investigated at 100 kHz. We can observe that $\boldsymbol{\delta t}$ and ***R*** have a linear relationship. As ***R*** approaches zero, we determined that the inherent FE-$\boldsymbol{P}$ switching speed exclusively restricts the NC effect. Finally, a 32 nm P(VDF-TrFE) LT provides a minimal *SS* of 23.39 mV/decade, 74.92% less than its CMOS counterpart. Therefore, the proposed organic MFM stack could open the path for developing beyond CMOS transistor technology operating in sub-60 mV/decade.

INDEX TERMS Landau transistor, Landau theory, negative capacitance effect, organic ferroelectric, sub-60 mV/decade.

I. INTRODUCTION

TODAY's intelligent society is defined by the internet, social media, and many fifth-generation computing electronic devices. A vast amount of data are produced and saved in many gigantic data centers and cloud computing systems. The emerging ultralow power (ULP) internet of things (IoT) devices may be able to assist in the optimization of everyday operations in several data centers across the world [1]–[3]. As a result, there is an urgent need to develop ULP IoT devices. It is possible to achieve this using super steep subthreshold swing (*SS*) transistors operating in the sub-60 mV/decade range at room temperature. However, standard CMOS transistors could not overcome the primary thermionic *SS* limitation of 60 mV/decade imposed by ''Boltzmann's Tyranny''. To overcome this Boltzmann's bottleneck, writing in Nano Letters [1], Salahuddin and Datta present a novel and exciting proposal for harnessing the negative capacitance (NC) effect by coupling a ferroelectric (FE)

layer to the channel of a standard CMOS transistor. As a result, in the current scenario, the NC field-effect transistor (NCFET), otherwise known as the "Landau transistor (LT)," has piqued the interest of many researchers around the world because it guarantees to reduce the supply voltage (V_G) requirement via an internal voltage amplification of the surface potential in the channel of the CMOS transistor. As a result, it is critical to exploit this NC effect at a low V_G, preferably less than 1 V.

Different research groups have demonstrated direct observations of the NC effect using oxide FEs like lead zirconate titanate, barium titanate, and hafnium zirconium oxide (HfZrO), considering a single domain (SD) state and a significantly higher V_G. For simplicity, most simulations of the NC effect assumed a steady-state environment. They ignored the impacts of the multidomain (MD) ferroelectricity, which is not valid in the real-time scenario [1]–[5]. Because the electric field varies when the drain voltage (V_D) is applied, causing non-uniform FE polarization (FE-P), the MD interaction factor is crucial in NCFET design [6], [7]. Moreover, the SD state shows a sharp FE-P switching, leading to overestimating the FE switching speed. Therefore, it is mandatory to incorporate the physics of the MD ferroelectricity in many simulations to accurately predict the FE and NCFET's performance. Again, the direct capturing of the NC effect at lower V_G as low as ±0.5 V and lower switched FE-P in both SD and MD states had not been investigated until now. In addition to this, understanding the physical cause of the NC effect in an organic FE poly(vinylidene fluoride-*co*-trifluoroethylene) [P(VDF-TrFE)]-based metal-FE-metal (MFM) capacitor and the evaluation of P(VDF-TrFE) amalgamation on the industry-standard short-channel CMOS transistor considering the MD ferroelectricity and dipole switching resistivity (ρ_{FE}) offered by the FE has not been extensively studied.

Therefore, in this study, we use an experimentally validated Ginzburg-Landau-Khalatnikov (GLK) technology computer-aided design (TCAD) model to investigate the transient nature of the proposed P(VDF-TrFE)-based MFM capacitor in both SD and MD conditions. P(VDF-TrFE) comprising VDF (70 mol%) and TrFE (30 mol%) is used as an organic FE material. First, we look at the FE properties of a solo MFM capacitor, taking into account quasistatic behaviors like polarization versus voltage (PV) and capacitance versus voltage (CV) curves. Following that, we looked into the systematic establishment of the MD and SD states as well as their FE-P switching under different bias conditions. Moreover, we investigate the non-quasistatic (NQS) behavior of the NC effect in both MD and SD states at an ultralow V_G. We show that the NC effect occurs when the FE-P is in the NC curvature of the organic FE's free energy landscape. It has been validated by considering a bipolar to unipolar pulsing approach. The impact of V_G, FE thickness, domain variations, external resistor (R), and ρ_{FE} on the transient NC effect are investigated. Finally, a 32 nm P(VDF-TrFE) LT is implemented by connecting the proposed MFM capacitor

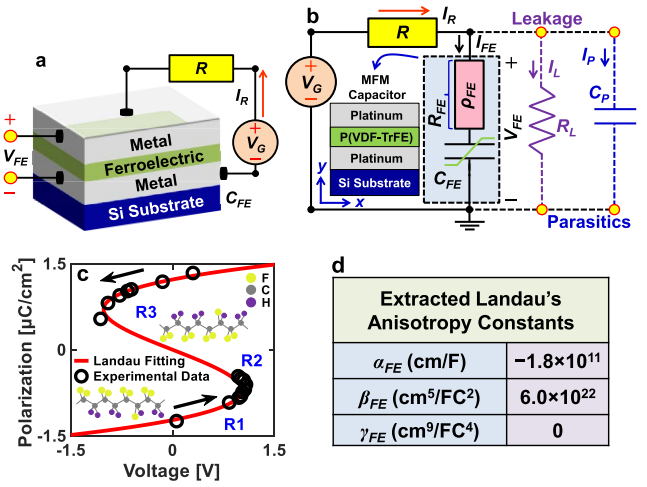

FIGURE 1. (a) Cartoon structure of the resistor-MFM capacitor (RC_{FE}) series circuit. V_G, R, I_R, V_{FE}, and C_{FE} are the supply voltage, resistor, total current, FE voltage, and capacitance across the MFM capacitor. (b) The equivalent circuit for the GLK simulation model of the RC_{FE} series circuit. I_{FE}, R_{FE}, and ρ_{FE} represent the FE current, internal resistance, and switching resistivity. R_L and C_P are the parasitic resistance and capacitance; I_L and I_P are the currents flowing through R_L and C_P. (c) Calibration of Landau's anisotropy constants with the reported experimental [8] PV curve of P(VDF-TrFE). (d) Extracted Landau's anisotropy constants of P(VDF-TrFE) material.

with an industry-standard CMOS transistor. The remainder of the article is structured as follows: in Section II, we discuss the strategy of TCAD simulation and the GLK model validation; in Section III, the obtained results are discussed considering different reported results in the literature. Finally, Section IV summarises the findings of our study.

II. TCAD SIMULATION AND MODEL CALIBRATION

The cartoon structure of the proposed MFM capacitor and the whole simulation setup to measure the NQS behavior of the NC effect are shown in Fig. 1(a). The TCAD simulation setup consists of an R in series with the MFM capacitor (RC_{FE}) and V_G of amplitude ±0.5 V operating at 100 kHz frequency. The equivalent circuit for the GLK simulation is shown in Fig. 1(b). The FE material employed in this study is a 10 nm thick P(VDF-TrFE) (70%-30%) sandwiched between the two noble metals [Platinum (Pt)] having the same thickness of 15 nm. We included the Pt electrodes to bypass many interlayer degradation issues related to the FE [9], [10]. In this article, the dielectric constant, $\varepsilon_{FE} = 10$, and the beta (β)-phase crystalline structure of the P(VDF-TrFE) (70%-30%) are used. This study has incorporated the Fermi-Dirac statistics and the GLK model in the TCAD environment. Finally, for every meshing point of the MFM capacitor, Poisson's and GLK equations are solved self-consistently.

Based on the electrostatics, the following relationship gives an overall free charge (Q_{FE}) of the MFM capacitor.

$$Q_{FE} = (\varepsilon_0 E_{FE} + P)\, A_{MFM} \tag{1}$$

where ε_0 is the free space permittivity, E_{FE} is the applied electric field, P represents the average FE-P, and A_{MFM} is

the MFM area. In Figs. 1(a) and 1(b), the total current (I_R) flowing through R in an RC_{FE} series circuit can be calculated by using the standard Kirchoff's law.

$$I_R = \frac{dQ_{FE}}{dt} = \frac{d}{dt}\left[\left(\varepsilon_0 \frac{V_{FE}}{t_{FE}} + P\right) A_{MFM}\right] \tag{2}$$

where V_{FE} stands for the voltage across the MFM capacitor and t_{FE} for the FE thickness. The phenomenological cause of the P(VDF-TrFE)'s FE-paraelectric phase transition at the Curie temperature is structurally similar to that of the displacive transition in oxide FE. This is because the microscopic origin of the FE-P switching in both P(VDF-TrFE) and the oxide FE is structurally identical [11]. Therefore, based on the Landau-Ginzburg-Devonshire theory of FE phase transition, the total Gibb's free energy of the P(VDF-TrFE) material can be expanded in order parameter, that is, FE-P, as shown in Eq. (3).

$$U_{FE} = \alpha_{FE} P^2 + \beta_{FE} P^4 + \gamma_{FE} P^6 + g_{FE} |\nabla P|^2 - E_{FE} P \tag{3}$$

Here, U_{FE} is the total free energy, $E_{FE}P$ is the electrostatic energy, and $g_{FE}|\nabla P|^2$ represents the Ginzburg energy. Again, α_{FE}, β_{FE}, and γ_{FE} are the material-dependent anisotropy constants, whereas g_{FE} is the domain coupling constant. Based on the time-dependent GLK equation of the FE, as shown in Eq. (4), we consider a dynamic model to study the MD effects having non-uniform FE-P and interaction among the domains. From Eqs. (3) and (4), the MD GLK equation is described in Eq. (5), which can strongly capture the FE-P switching in the MFM capacitor [6], [7], [12]–[17].

$$\rho_{FE}\left(\frac{dP}{dt}\right) + \nabla_P U_{FE} = 0 \tag{4}$$

$$V_{FE} = t_{FE}\left[\rho_{FE}\left(\frac{dP}{dt}\right) - 2g_{FE}\left(\nabla^2 P\right) + 2\alpha_{FE} P + 4\beta_{FE} P^3 + 6\gamma_{FE} P^5\right] \tag{5}$$

Therefore, based on Eq. (5), the MFM capacitor is modeled by a series combination of internal resistance (R_{FE}) and a non-linear FE capacitor (C_{FE}) characterized by the GLK parameters. Therefore, it is necessary to extract the GLK parameters of the FE material. For this study, we have specifically chosen P(VDF-TrFE) as the FE material because it is the only FE reported so far that can flip the dipole at lower V_G and saturated well below 3 μC/cm^2 [5]. As shown in Fig. 1(c), the black color circular points are the sampled experimental data [8]. Several important points on the experimental curves are picked to capture its S-shape PV curve. The points on the negative-slope curve are chosen with a smaller step (see region R2) because the NC effect is largely reliant on the α_{FE} parameter at low FE-P. Positive slope points with a larger step are chosen to illustrate the trend at large FE-P, which is controlled by β_{FE} (see regions R1 and R3). Using the curve fitting technique [5], the values of α_{FE}, β_{FE}, and γ_{FE} for P(VDF-TrFE) are extracted as, $\alpha_{FE} = -1.8 \times 10^{11}$ cm/F, $\beta_{FE} = 6.0 \times 10^{22}$ cm^5/FC^2, and $\gamma_{FE} = 0$ cm^9/FC^4 from the experimental data [8] [see Fig. 1(d)], assuming that the P(VDF-TrFE) undergoes a second-order phase transition, resulting in $\alpha_{FE} < 0$, $\beta_{FE} > 0$, and $\gamma_{FE} = 0$ [4], [12], [13]. The simulated red S-shaped curve employing these extracted values, especially in the NC region of the ascending branch, fit well with the experimentally recorded data, as shown in Fig. 1(c). The FE capacitance, C_{FE} is indicated by the slope at each position along the Landau path. From Eq. (5), one can write the relationship between C_{FE} and P in steady-state conditions, as shown in Eq. (6).

$$C_{FE} = \frac{1}{\left(2\alpha_{FE} t_{FE} + 12\beta_{FE} P^2 t_{FE} + 30\gamma_{FE} P^4 t_{FE}\right)} \tag{6}$$

Since the FE materials are insulators by nature, we have taken the value of internal resistivity, $\rho_{FE} = 100$ kΩcm, as an arbitrary fitting parameter [3]. We set the value of g_{FE} to 1×10^{-3} cm^3/F to ensure adequate interaction among the domains [13], [14]. In the SD state, we assume that the FE-P is equally distributed throughout the FE, and $g_{FE} = 0$.

III. SIMULATION RESULTS AND DISCUSSION

A. ORGANIC MFM CAPACITOR: FERROELECTRICITY

To ascertain the feasibility of ferroelectricity in the proposed MFM capacitor, we simulated its electrical properties at room temperature. Fig. 2(a) shows the quasistatic response of the proposed isolated MFM capacitor. The remanent polarization [$P_r = (P_{r+} - P_{r-})/2 = 1.25$ μC/cm^2] and coercivity [$V_C = (V_{C+} - V_{C-})/2 = 0.34$ V] of the isolated MFM has been extracted from Fig. 2. The proposed MFM capacitor with P(VDF-TrFE) can achieve a phenomenal V_C reduction of about 84.89% from its HfZrO [17] counterpart. At 100 kHz, the CV characteristics of the isolated MFM capacitor cruising from 0 to 34.16 fF are shown in Fig. 2(b). The charge versus voltage (QV) curve is used to generate the CV curve. The butterfly-shaped CV characteristics and PV hysteresis loop prove ferroelectricity in the proposed isolated MFM capacitor.

B. FE-P SWITCHING IN SD AND MD STATE

The process of FE-P switching dynamics according to the FE's SD and MD states is shown in Fig. 3. In the SD isolated MFM capacitor, just after forming a single reverse domain nucleus in the FE layer, it continues to grow in the transverse direction without interacting with other domains (see inset 1 in Fig. 3). As a result, the FE-P switches abruptly near the V_C, and a sharp PV curve is observed. On another note, for MD GLK modeled isolated MFM capacitor, if an external V_G is applied to the FE layer (see inset 2 in Fig. 3), various domain nuclei are created at random and grow independently. Since the applied V_G and the FE-P switching time of the numerous domain nuclei have a specific distribution, the PV curve shows a smooth slant, indicating that the FE-P switching occurs one after another before applying the V_C. Using the Landau-Lifshitz-Kittle (LLK) rule [18], the estimated domain size is approximately 3.16 nm.

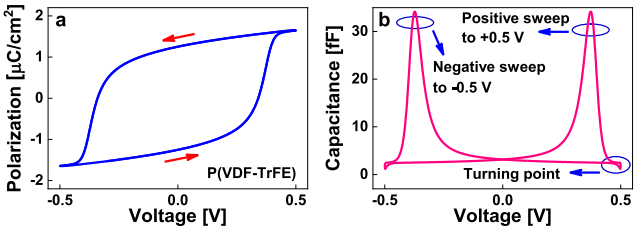

FIGURE 2. **(a) PV curve depicting the quasistatic response of the proposed MFM capacitor. (b) CV curve of an isolated MFM capacitor.**

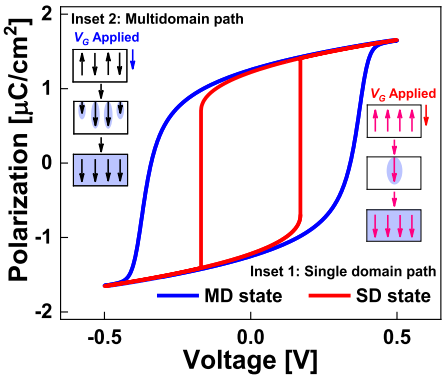

FIGURE 3. **PV characteristics of different states of FE-*P* in an MFM capacitor at 300 K. Inset 1 indicate the FE-*P* switching process in the SD path, and inset 2 indicates the switching process in an MD path.**

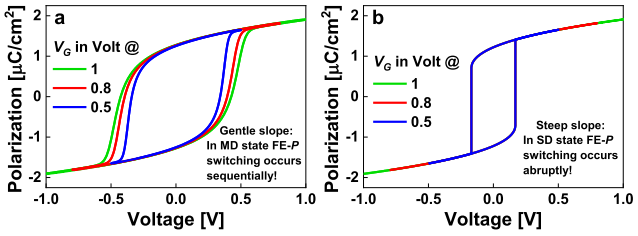

FIGURE 4. **Systematic formation of (a) MD path and (b) SD path at different V_G.**

The inhomogeneously distributed domains (FE-$P\uparrow$ and FE-$P\downarrow$) have approximately equal width under zero bias conditions, and zero net FE-P is achieved by having the same FE-$P\uparrow$ and FE-$P\downarrow$. As a corollary, the macroscopic charge-neutral interfaces are generated [19]. Therefore, the FE-P switching is determined by the GLK parameters of the FE material. Furthermore, we investigate the influence of V_G's various values on the quasistatic response of the PV curve, considering both MD and SD states. The simulated PV curve of the MFM capacitor in both MD and SD states at different bias conditions is shown in Figs. 4(a) and 4(b). From Fig. 4(a), it is evident that the PV curve shows a gentle slope (at 0.5, 0.8, and 1 V), meaning that the FE-P switching takes place sequentially. This is due to the fact that in the MD state, several domains are created at random and expanded individually. Whereas in the case of the SD state, we observe a sharp fall of the FE-P switching around the V_C, and hence a steep slope PV curve is expected for an SD state because the domain grows without nucleating with other domains. Finally, it is worth noting that the V_C of the MFM capacitor in the MD state (0.34 V) is larger than the V_C of the MFM capacitor in the SD state (0.17 V) at a driving voltage of ± 0.5 V. This is attributable to why the FE-P switching occurs more abruptly in an SD state than that of the MD state.

C. NQS BEHAVIORS OF NC EFFECT AND ITS PHYSICAL CAUSE

We scrutinize the transient nature of the RC_{FE} series circuit by applying a step bipolar signal drifting from $-0.5 \rightarrow +0.5$ V with $R = 30$ MΩ at room temperature. The NC effect is observed by simulating the voltage (V_{FE}) and charge (Q_{FE}) across the MFM capacitor, considering both MD [see Fig. 5(a)] and SD [see Fig. 5(b)] states. In Fig. 5(a), we notice opposite signs of changes in V_{FE} and Q_{FE} during the time frame JO and HN. Similar changes are observed in the SD state but with an abrupt change, as shown in regions NC1 and NC2 of Fig. 5(b). These phenomena indicate that the FE-P crosses through the NC region of the thermodynamic free energy profile where the C_{FE} is negative ($dQ_{FE}/dV_{FE} < 0$). As a result, for the first time, we can capture the NQS behavior of the NC effect at ± 0.5 V, which is ideal for ULP CMOS technology. The total current I_R flowing through R can be calculated with $I_R = [(V_G - V_{FE})/R]$. Moreover, the overall charge ($Q_{Overall}$) can be obtained by integrating I_R as a function of time, as shown in Eq. (7).

$$Q_{Overall} = \int I_R(t)\, dt \tag{7}$$

If the value of $I_R(t)$ is known, then using a fundamental network theorem, we can calculate Q_{FE} as a function of time from the simulated voltage transients, as shown in Eq. (8).

$$Q_{FE}(t) = \left[Q_{FE}(t=0) + \frac{1}{R}\int_0^t \{V_G(t) - V_{FE}(t)\}\, dt - C_P V_{FE}(t) \right] \tag{8}$$

Here, $Q_{FE}(t=0)$ in Eq. (8) represents the initial Q_{FE} of the MFM capacitor at $t = 0$. The leakage current (I_L) contribution is neglected because it is relatively minimal compared to I_R. Further, C_P's effects are negligible since Q_{FE} is comparatively higher than the charge stored at C_P. It is essential to understand the step-by-step transient response of the proposed MFM capacitor. Therefore, the transient response is described in three stages—

Stage 1 (0 to J time-segment): Stage 1 shows the initial response of the V_{FE} similar to that of the standard dielectric charging curve. This is because of the non-FE-P states, which are quasistatic, depending on the time frame of the V_G rise time. Hence, there is no evidence of the NC effect at this stage. The time of "stage 1" may be expressed as the sum of the signal rising time (t_r) and the time constant $[(R + R_{FE})C_{FE}]$, that is, $[t_r + k.(R + R_{FE})C_{FE}]$. In this case, $k.(R + R_{FE})C_{FE}$

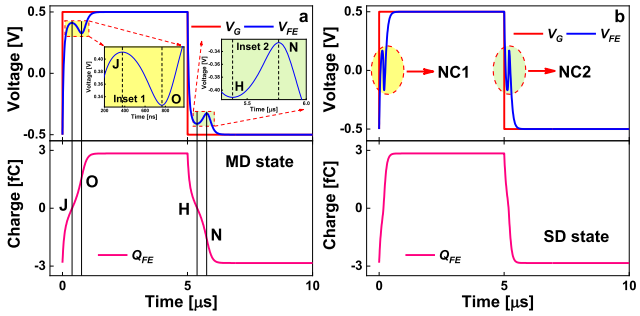

FIGURE 5. Transient NC effect of the RC_{FE} series circuit to a bipolar input signal V_G: −0.5 → +0.5 V: (a) MD condition assuming a non-uniform FE-*P*. A smooth V_{FE} response is observed as the entire FE-*P* switches sequentially. NC effect is observed during JO and HN time segments. (b) SD condition considering a uniform FE-*P*. In this case, a sharp fall in V_{FE} is observed. NC effect is observed during the time segment indicated by the regions NC1 and NC2, respectively.

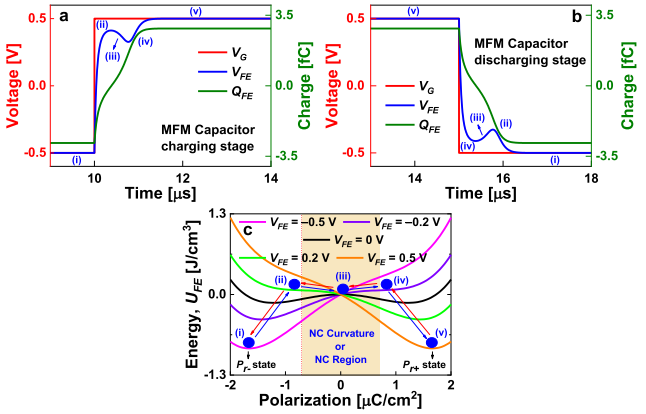

FIGURE 6. Voltage transient (V_{FE}) of the MFM capacitor during (a) Charging stage. (b) Discharging stage. (c) The thermodynamic free energy landscapes at various time steps when charging and discharging the MFM capacitor. The blue arrow represents the charging stage's FE-*P* switching direction, while the red arrow indicates the discharging stage's FE-*P* switching direction.

represents the effective RC_{FE}, where coefficient k shows the impact of t_r on $(R + R_{FE})C_{FE}$.

Stage 2 (J to O time-segment): After stage 1, when the input step signal is higher than V_C, the FE-*P* starts switching its direction sequentially as the entire FE-*P* does not switch abruptly during the process, and as a result, we notice that the V_{FE} increases till J point and starts decreasing in a much gentle path up to a point O [see inset 1 in Fig. 5(a)]. In the same JO time segment, the Q_{FE} increases, and vice-versa occurs in the HN time-segment [see inset 2 in Fig. 5(a)], leading to the NC effect. Meanwhile, in the SD state, since the entire MFM capacitor is supposed to have a uniform distribution of FE-*P*, and the entire FE-*P* needs to switch, therefore the V_{FE} drops sharply, as shown in regions NC1 and NC2 [see Fig. 5(b)]. Finally, when considering the NC duration during FE-*P* switching based on *R* change, the lengths of stage 1 and stage 2 are nearly identical. As *R* increases, the time of both stages 1 and 2 increases (more detail in section F). Therefore, the time of stage 2 can be expressed as $[t_r + k.(R+R_{FE})C_{FE}] < t \leq 2[t_r + k.(R + R_{FE})C_{FE}]$.

Stage 3 (O to 5 μs time-segment): It occurs just after completing the FE-*P* switching, and the charging of the MFM starts just like a normal capacitor in the MD state, as shown in Fig. 5(a). Similar events occur in the SD state, although at a considerably quicker rate than in the MD state, as shown in Fig. 5(b). Finally, the time of stage 3 can be represented as $2[t_r + k.(R+R_{FE})C_{FE}] < t < (t_p/2)$. Here, t_p represents one cycle of the pulse signal.

Figs. 6(a) and 6(b) show that the NC effect occurs only when the FE-*P* is in the negative curvature or NC region of the thermodynamic free energy landscape. This relationship can be seen in Fig. 6(c), where the thermodynamic free energy profiles at various time steps are given during the charging and discharging of the MFM capacitor. The charging behavior of the MFM capacitor behaves like a positive linear capacitor, especially during the time steps (i) to (ii) and then from (iv) to (v), as shown in Fig. 6(a), whereas during the discharging stage the MFM capacitor acts like a positive capacitor during (v) to (iv) and (ii) to (i) time steps [see Fig. 6(b)]. This is because of the dielectric response of the MFM capacitor, meaning that the infinitesimal change in charge (dQ_{FE}) and infinitesimal change in the voltage (dV_{FE}) have the same sign. Furthermore, this process can be understood from the direct mapping of the transient V_{FE} to the thermodynamic energy profile, where one can see that the state of the FE-*P* at the said time steps are in the positive capacitance region, implying that the FE-*P* states are sitting on the stable state (P_{r-} state) or (P_{r+} state) or on the edge of the NC curvature.

However, when the V_{FE} across the MFM capacitor is higher than V_C, the thermodynamic free energy profile is fully tilted to the right for +0.5 V and to the left for −0.5 V. As a result, the FE-*P* rolls down the hill, passing the NC curvature/region where the C_{FE} is negative, meaning that dQ_{FE} and dV_{FE} are in the opposite direction, that is, $(dQ_{FE}/dV_{FE}) < 0$ during the time step (iii), (this phenomenon occurs during both charging and discharging stages of the MFM capacitor). Therefore, while switching the FE-*P* from P_{r+} state to P_{r-} state and vice-versa, the FE-*P* crosses through the NC region, and thus the NC effect occurs. Finally, to validate the physical cause of the NC effect in the MFM capacitor, we have adopted a bipolar to unipolar pulsing technique, in which two successive unipolar DC pulses ranging from $0 \rightarrow +0.5\ \text{V} \rightarrow 0$ is applied initiated by a bipolar AC signal (V_G: $-0.5 \rightarrow +0.5$ V). The NC effect is only visible during the first unipolar pulse and disappears in successive positive unipolar DC pulses, as shown in Fig. 7(a). This is because the MD FE-*P* switching occurs in the first unipolar pulse, whereas, during the second unipolar pulse, the MD FE-*P* switching does not occur since they are already positively aligned with the applied E_{FE} in the preceding pulse resulting in the absence of the NC effect. It can be understood from its corresponding dynamic PV loop where the FE-*P* switching is

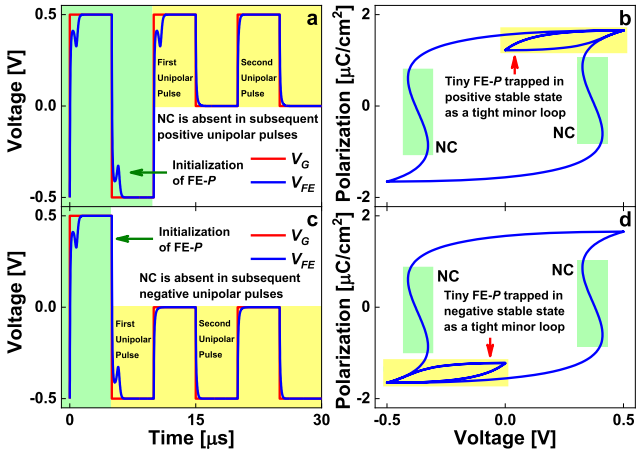

FIGURE 7. **(a) Voltage transients in response to a unipolar step DC pulse (V_G: 0 → +0.5 V → 0) initiated by a bipolar AC signal (V_G: −0.5 → +0.5 V). (b) Dynamic PV trajectory indicating the tiny FE-*P* trapped in the positive stable state as a tight minor loop. (c) Voltage transients in response to a unipolar step DC pulse (V_G: 0 → −0.5 V → 0) initiated by a bipolar AC signal (V_G: −0.5 → +0.5 V). (d) Dynamic PV trajectory indicating the tiny FE-*P* trapped in the negative stable state as a tight minor loop.**

TABLE 1. **Performance comparison with reported MD NC effect.**

Parameters →	FE Material	Min. V_G for NC (V)	Freq. (kHz)	$2P_r$ (μC/cm²)	Intrinsic δt (ns)
This work	P(VDF-TrFE)	±0.5	100	2.5	300
[28]	HfZrO	±5.0	50	24	41.4

trapped in the positive stable state as a tight minor loop not strong enough to induce the NC effect [see Fig. 7(b)].

Again, a similar simulation strategy with a unipolar DC pulsing (0 → −0.5 V → 0) is performed in the negative direction, and its impact on the NC effect is illustrated in Fig. 7(c). As illustrated in Figs. 7(c) and 7(d), the expected NC effect behaviors are observed, and the ultimate rationale for such phenomena may be deduced from its dynamic PV curve. We cannot observe the apparent NC effect after the first unipolar pulse in the negative direction because the FE-*P* is trapped in the negative stable state as a tight minor loop. This excellent relationship between the FE-*P* switching and the transient response demonstrates that the NC effect is caused by intrinsic FE-*P* switching dynamics rather than any external dynamics or charged faults in the system.

D. IMPACT OF t_{FE} AND DOMAIN VARIATIONS ON NC EFFECT

Examining the NC effect at an ultrathin t_{FE} is crucial. As a result, we investigate how t_{FE} affects the transient NC effect at ambient temperature, assuming that the thickness of the P(VDF-TrFE) is thinned down to 2.5 nm, in spite of the practical difficulties to achieve such dimensions using current fabrication technology. As the t_{FE} gets thinner in the MFM capacitor, the effects of depolarization become more evident in degrading the FE's ferroelectricity. As a corollary, the change in FE-*P* with time (*dP/dt*) becomes unimportant

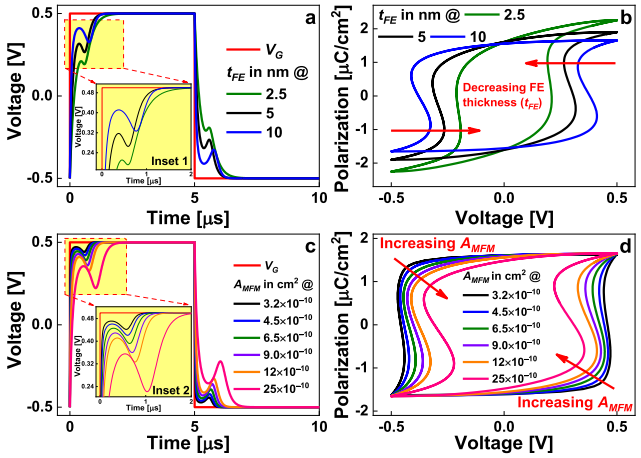

FIGURE 8. **(a) Transient NC effect of RC_{FE} series circuit at various values of t_{FE}. (b) Dynamic PV curve at different t_{FE}. (c) Transient NC effect of RC_{FE} series circuit at various A_{MFM}. (d) Dynamic PV curve indicating the NC effect voltage window (δV_{NC}) at different A_{MFM}.**

with the rise in the depolarization electric field (E_{Dep}) [20]. Therefore, we observe a weaker NC effect as t_{FE} reduces from 10 to 2.5 nm, as shown in Fig. 8(a). The dynamic hysteresis loop [see Fig. 8(b)] can explain the weaker NC effect, where the NC effect voltage window (δV_{NC}) starts diminishing with the reduction of the t_{FE} and eventually starts behaving like an SD state. Again, as the t_{FE} reduces, the domain state changes from hard to soft, meaning that the domains are no longer physically separable entities [20], [21]. As a result, the FE-*P* switching takes place at much lower voltages with a lesser NC effect. However, the domain state switches to an SD state after a critical thickness.

Moreover, from [20] and [22], it is well known that as the t_{FE} layer decreases, the E_{Dep} on the MFM capacitor increases. As a result, as shown in Fig. 8(b), as t_{FE} decreases, the PV hysteresis loop loses its typical squareness and begins to slant more observably in the counterclockwise direction, increasing the value of the *FE* saturation polarization (P_S). The phenomenon can be understood by assuming that a very thin oxide layer forms while the *FE* P(VDF-TrFE) layer is deposited on the metal electrode. If the *FE* layer and the surface oxide layer are thought of as a series system, the E_{Dep} can be expressed as

$$E_{Dep} = \frac{P_S \times t_{ox}}{\{\varepsilon_0 (\varepsilon_{ox} t_{FE} + \varepsilon_{FE} t_{ox})\}} \tag{9}$$

where t_{ox} is the oxide thickness, and ε_{ox} represents the oxide permittivity. From Eq. (9), P_S can be expressed in terms of E_{Dep} and t_{FE}, as shown in Eq. (10).

$$P_S = \frac{E_{Dep} \{\varepsilon_0 (\varepsilon_{ox} t_{FE} + \varepsilon_{FE} t_{ox})\}}{t_{ox}} \tag{10}$$

Because we already know that E_{Dep} increases as t_{FE} decreases, it follows from Eqs. (9) and (10) that P_S increases as t_{FE} decreases. The phenomenon depicted in Fig. 8(b) is consistent with the experimental results reported in [22] and [23].

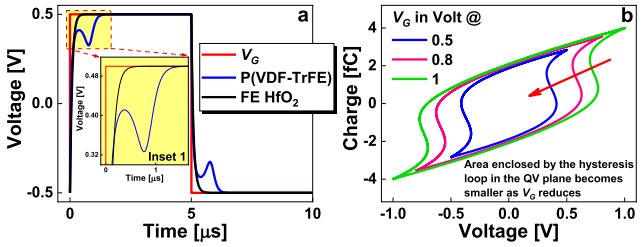

FIGURE 9. (a) Transient NC effect of RC_{FE} series circuit using P(VDF-TrFE) and FE HfO_2 [24]. (b) Influence of V_G on the dynamic charge versus voltage (QV) loop of the proposed RC_{FE} series circuit.

Next, we investigate the influence of the domain variations on the transient behavior of the RC_{FE} series circuit. Therefore, various A_{MFM} (3.2×10^{-10}, 4.5×10^{-10}, 6.5×10^{-10}, 9.0×10^{-10}, 12×10^{-10}, and 25×10^{-10}cm^2, respectively) are considered in this study. The simulated transient NC effect response of the RC_{FE} series circuit and its corresponding dynamic PV loop indicating the δV_{NC} of the MFM capacitor is depicted in Figs. 8(c) and 8(d), respectively. From Fig. 8(c), we notice that the six different A_{MFM} show different transient responses of V_{FE}; C_{FE} charges gradually as the A_{MFM} accentuates from 3.2×10^{-10} to 25×10^{-10}cm^2. Since the V_G's operating frequency is fixed at 100 kHz, it is evident that the smallest A_{MFM} (3.2×10^{-10}cm^2) tends to charge more rapidly than the other larger MFM capacitors. The explanation for this could be the presence of varying domain counts in the P(VDF-TrFE) material employed as an organic FE in the MFM capacitor. Several domain counts are involved where the domain velocity limits the dynamic FE-P switching speed as the A_{MFM} becomes larger. As a result, the larger MFM capacitor charges slowly [inset 2 in Fig. 8(c)]. Similarly, the δV_{NC} increases as the A_{MFM} accentuate from 3.2×10^{-10} to 25×10^{-10}cm^2 [see Fig. 8(d)]. Since the RC_{FE} time constant is crucial to fully understand the charging behavior of any MFM capacitor, its value can be easily manipulated by tuning the A_{MFM}.

E. NC EFFECT IN OXIDE FE AND P(VDF-TrFE)-BASED RC_{FE}

The emergence of a damaged interlayer is highly likely possible in the process of forming the conventional oxide FEs because of the very high ambient oxidation temperature. As a result, a more considerable amount of V_G is wasted, and only a tiny amount of V_G is available across the MFM capacitor. The dead interlayer's emergence can be suppressed by employing the P(VDF-TrFE) instead of the oxide FEs because of its relatively low ambient oxidizing temperature, low leakage current, good reliability, and CMOS compatibility [8]–[10]. Therefore, it is necessary to investigate the NC effect on the RC_{FE} series circuit using different FEs such as P(VDF-TrFE) and FE hafnium dioxide (HfO_2). The simulation parameters of FE HfO_2 are directly taken from [24].

We notice that the proposed P(VDF-TrFE)-based MFM capacitor can capture the NC effect at minimum V_G as low as 0.5 V [see inset 1 in Fig. 9(a)]. In contrast, the FE HfO_2-based

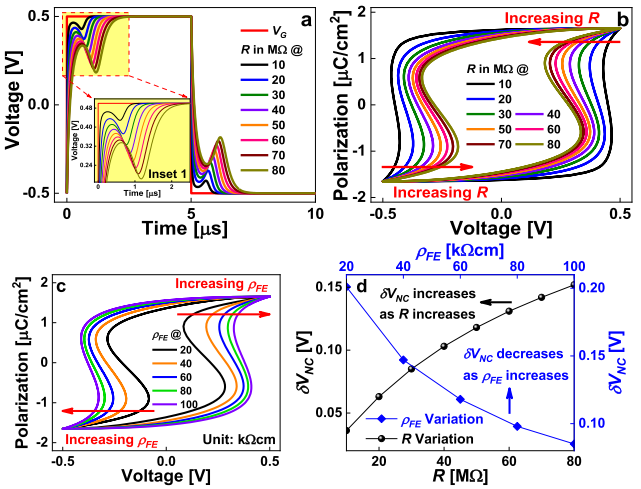

FIGURE 10. (a) Transient NC effect of RC_{FE} series circuit for different R. (b) Dynamic PV curve for different R values. (c) Dynamic PV curve for different values of ρ_{FE}. (d) δV_{NC} for different R and ρ_{FE}.

MFM capacitors fail to harness the NC effect at 0.5 V. The reason is attributable to the higher V_C of the FE HfO_2 (0.7 V) higher than V_G, meaning that the voltage drop across the FE HfO_2-based MFM capacitor is not strong enough to induce the dynamic FE-P switching in the FE domains for proper screening of FE-P in the NC region. As a corollary, the voltage change across the FE HfO_2-based MFM capacitor has the same sign as the V_G, which rules out the NC effect. The exponential rise or fall of the voltage across the FE HfO_2-based MFM capacitor along with the time scale can be seen in Fig. 9(a), which behaves like a regular linear positive capacitor. Furthermore, the impact of different values of V_G on the dynamic QV curve of the proposed MFM capacitor-based RC_{FE} series circuit is shown in Fig. 9(b). We observe that as the V_G's value reduces from 1 to 0.5 V, the energy dissipation (ED) reduces dramatically from 5.9 to 2.7 fJ, respectively. The energy is dissipated as heat through R, which is calculated using Eq. (11).

$$Energy_{Cycle} = \int_{loop} VdQ \tag{11}$$

Therefore, the proposed P(VDF-TrFE)-based MFM capacitor could capture the NC effect at a much smaller hysteresis loss leading to a minimum ED of ∼2.7 fJ. The performance comparison with the previously reported MD NC effect is shown in Table 1. The proposed MFM's P_r is relatively smaller than its inorganic FE counterpart (HfZrO). This is because organic FEs like P(VDF-TrFE) generally have smaller P_r [25], and it is the only known FE that could exhibit ferroelectricity and saturate comfortably below 3 μC/cm^2 [8], [26]. The value of the P(VDF-TrFE)'s P_r shown in Table 1 is consistent with the reported experimental P_r [8]. Finally, the V_C and P_r values presented in Table 1 may be effectively balanced by simply changing the sweeping voltage range because V_C and P_r are dependent on the sweeping voltage range [27].

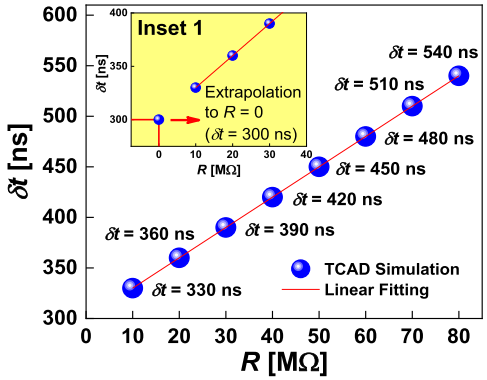

FIGURE 11. NC time (δt) as a function of R for the MFM capacitor.

F. IMPACT OF R AND ρ_{FE} ON NC EFFECT

To fully grasp the impact of screening charge compensation on the NC effect, we investigate the change in the transient NC effect and dynamic hysteresis loop with different R values ranging from 10 to 80 MΩ. Fig. 10(a) shows the transient NC effect of the proposed MFM capacitor in response to a V_G: $-0.5 \rightarrow +0.5$ V. We carefully scrutinize the transient NC effects and found that as R increases, the FE-P switching occurs at lower V_{FE}, and charge compensation occurs for a longer time, leading to a more gentle NC effect [see inset 1 in Fig. 10(a)]. Further, we observe that the NC time (δt) also increases as R increases. Note that a considerably higher value of R might lead to the NC effect's disappearance because of smaller V_{FE} lesser than the V_C of the MFM capacitor. On the contrary, employing a much smaller R-value could make the NC effect too tiny to be observable. Therefore, R's careful tuning is required because not all the RC_{FE} series circuit shows the NC effect phenomena [28].

Fig. 10(b) predicts an increasing trend of δV_{NC}, whereas, Fig. 10(c) predicts a decreasing trend of δV_{NC}. To see this variation, δV_{NC} for different values of R and ρ_{FE} are shown in Fig. 10(d). We note from Fig. 10(d) that δV_{NC} increases monotonically as R accentuate, whereas the value of δV_{NC} strictly decreases with the increase in ρ_{FE}. Here, the range of the FE-P of the NC effect remains unchanged. The trends in Fig. 10(d) are consistent with the results reported in [4], [29].

Further, to validate the implications of the time constant RC_{FE} on the transient NC effect, we have extracted the δt of the MFM capacitor for several values of R from Fig. 10(a). Fig. 11 shows a linear decrease of δt down to 330 ns as R is reduced to 10 MΩ. In Fig. 11, we can see that the δt varies linearly with R. This points out that the δt is directly controlled by the R and not by the FE material-dependent intrinsic switching speeds of the MFM capacitor. Finally, we can see from inset 1 in Fig. 11 that the δt versus R curve intercepts the $R = 0$ line at $\delta t = 300$ ns, which is very close to $\delta t = 0$ but not lesser than 41.4 ns the intrinsic δt of the FE oxide HfZrO reported in [28]. This might be because of the smaller internal resistivity offered by HfZrO. Therefore, the maximum intrinsic switching speed of the P(VDF-TrFE) and HfZrO without any delay from the external circuitry is about 3.33 and 24.15 MHz, respectively. This suggests that the δt is now limited only by the FE-P switching speed when R tends to zero limits. Although the proposed P(VDF-TrFE)-based MFM device could harness the NC effect at a low V_G (0.5 V) and a low ED (∼2.7 fJ), the intrinsic switching speed of the oxide FE HfZrO is faster than the P(VDF-TrFE), as shown in Table 1.

TABLE 2. Simulation parameters for P(VDF-TrFE) LT.

Baseline CMOS Transistor	
Channel length (L)	32 nm
Channel width (W)	1 μm
Effective oxide thickness (EOT)	1.15 nm
Junction depth (X_j)	10 nm
Oxide dielectric constant (ε_{ox})	3.9
Free space permittivity (ε_0)	8.854×10^{-14} F/cm
Doping density of substrate (N_{sub})	4.12×10^{18} cm^{-3}
Mobility of charge carrier (μ)	500 cm^2/Vs
Organic Ferroelectric Parameters	
Ferroelectric thickness (t_{FE})	10 nm
P(VDF-TrFE) dielectric constant (ε_{FE})	10
α_{FE}	-1.8×10^{11} cm/F
β_{FE}	6.0×10^{22} cm^5/FC^2
γ_{FE}	0 cm^9/FC^4
ρ_{FE}	100 kΩcm
g_{FE}	1×10^{-3} cm^3/F

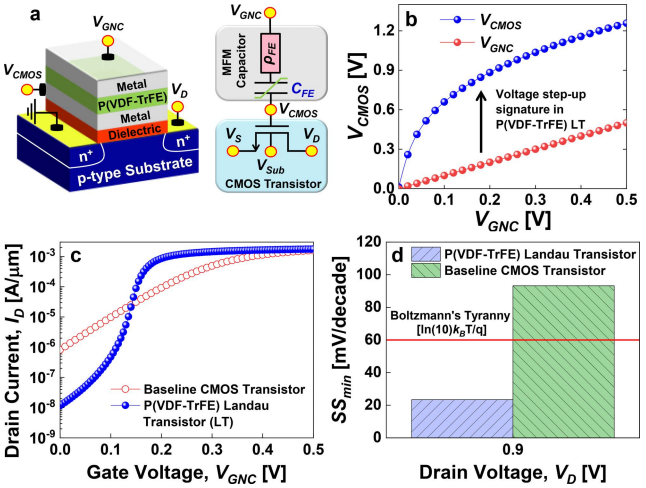

FIGURE 12. (a) Cartoon structure of the P(VDF-TrFE) LT and its equivalent circuit symbol. (b) Voltage step-up signature in P(VDF-TrFE) LT. (c) Drain current versus gate voltage characteristics of the P(VDF-TrFE) LT and the baseline CMOS transistor with $V_D = 0.9$ V. (d) SS_{min} of the proposed P(VDF-TrFE) LT and the baseline CMOS transistor with $V_D = 0.9$ V.

G. P(VDF-TrFE) LANDAU TRANSISTOR (LT)

The best way to realize how the proposed MFM capacitor alters the baseline CMOS transistor is to look at the SS. Therefore, a P(VDF-TrFE) LT is implemented by simply connecting the MFM capacitor in series with an industry-standard CMOS transistor. Fig. 12(a) shows the cartoon structure of the P(VDF-TrFE) LT and its equivalent circuit symbol. The optimal simulation parameters of the P(VDF-TrFE) LT in a 32 nm process technology [30], [31] are shown in Table 2.

For the simulation of the P(VDF-TrFE) LT, Fermi-Dirac statistics is assumed, standard Shockley-Reed-Hall doping dependence model and the drift-diffusion model along with the standard MD GLK model is used. The voltage step-up signature induced by the NC effect in P(VDF-TrFE) LT is shown in Fig. 12(b). For $L = 32$ nm and $W = 1$ μm, we simulated the drain current versus gate voltage characteristics of the proposed P(VDF-TrFE) LT and the baseline CMOS transistor with $V_D = 0.9$ V. We obtained the average SS of 39.48 and 104.98 mV/decade for the proposed P(VDF-TrFE) LT and the baseline CMOS transistor, respectively, from Fig. 12(c). For the P(VDF-TrFE) LT, the minimum SS (SS_{min}) reduces to about 23.39 mV/decade [see Fig. 12(d)], much lower than that of the baseline CMOS transistor (93.25 mV/decade). Compared to the off-state current (I_{off} = 820.3 nA/μm) of the CMOS transistor, the P(VDF-TrFE) LT's transfer characteristics show a much lower I_{off} (11.69 nA/μm). Finally, a high on/off current ratio of 1.503×10^5 is obtained in the P(VDF-TrFE) LT, much higher than the baseline CMOS transistor with an on/off current ratio of 1.952×10^3. Furthermore, the proposed P(VDF-TrFE) LT's SS_{min} is 57.63 % and 53.40 % lower than the MD FE-based transistors reported in [6] and [32], respectively. These findings support the hypothesis that the proposed MD MFM capacitor with the NC effect could pave the way for a sub-60 mV/decade transistor technology.

IV. CONCLUSION AND FUTURE SCOPE

The following conclusions can be derived from this article examining the operation of the P(VDF-TrFE)-based MFM device and its application to the Landau transistor.

(1) In summary, by performing the experimentally validated GLK model-based TCAD simulation, we can harness the NC effect at lower V_G as low as $\pm$0.5 V in an RC_{FE} series circuit with a little ED of $\sim$2.7 fJ, which is still a hurdle for regular FE HfO_2-based MFM capacitors.

(2) An isolated P(VDF-TrFE)-based MFM capacitor achieves an 84.89% reduction in V_C when compared to oxide FE (HfZrO) [17].

(3) The NQS behavior of the NC effect in an RC_{FE} series circuit considering both MD and SD states is illustrated. We observe a gentle FE-P switching for the MD state, whereas an abrupt FE-P switching is observed for the SD state.

(4) Subsequently, we observe that the physical cause of the NC effect is linked directly to the FE-P switching dynamics of the MFM capacitor and not because of any extrinsic system defects. Moreover, it is justified by its dependence on V_G, t_{FE}, domain variations, R, and ρ_{FE}, respectively.

(5) Interestingly, we found MD behavior even at an ultra-scaled MFM capacitor having A_{MFM} of 3.2×10^{-10}cm^2. However, after a critical t_{FE} of 2.5 nm, the MFM capacitor starts behaving like an SD state.

(6) Moreover, we notice a linear dependence of the δt with R; the value of δt at $R = 0$ is very close to zero, meaning that the intrinsic FE-P would only limit the δt.

(7) Ultimately, the proposed MFM capacitor with a switched charge density (P_r) of 1.25 μC/cm^2 comparable to the CMOS transistor's channel charge density of 1.6 μC/cm^2, and V_C of 0.34 V could be used to solve the major issues related to the capacitance matching in LT design at minimal ED.

(8) We tried to achieve lower driving voltage via the reduction in V_C, which is really useful for voltage scaling; however, sacrificing with the thicker EOT due to the rule of the capacitance matching. This requires more study maybe double switching of gate voltage is preferred to monitor the capacitance matching.

(9) The P(VDF-TrFE) LT provides an SS_{min} of 23.39 mV/decade, 74.92% lower than its CMOS equivalent. Compared to the conventional CMOS transistor [see Fig. 12(c)], the improved I_{off} and on/off current ratio is confirmed.

Therefore, the proposed P(VDF-TrFE) LT operating at sub-60 mV/decade could be a significant step forward in developing a new beyond CMOS transistor technology. Our study suggests that a practical technology device menu may need to include the baseline CMOS transistors and LTs, which poses additional co-optimization issues and should be the primary focus of future research in NC-based transistors.

REFERENCES

[1] S. Salahuddin and S. Datta, "Use of negative capacitance to provide voltage amplification for low power nanoscale devices," *Nano Lett.*, vol. 8, no. 2, pp. 405–410, Feb. 2008, doi: 10.1021/nl071804g.

[2] M. Kobayashi, "A perspective on steep-subthreshold-slope negative-capacitance field-effect transistor," *Appl. Phys. Exp.*, vol. 11, no. 11, Nov. 2018, Art. no. 110101, doi: 10.7567/APEX.11.110101.

[3] A. I. Khan *et al.*, "Negative capacitance in a ferroelectric capacitor," *Nature Mater.*, vol. 14, no. 2, pp. 182–186, Feb. 2015, doi: 10.1038/nmat4148.

[4] A. K. Saha, S. Datta, and S. K. Gupta, "'Negative capacitance' in resistor-ferroelectric and ferroelectric-dielectric networks: Apparent or intrinsic?" *J. Appl. Phys.*, vol. 123, no. 10, Mar. 2018, Art. no. 105102, doi: 10.1063/1.5016152.

[5] Y. Li, Y. Lian, K. Yao, and G. S. Samudra, "Evaluation and optimization of short channel ferroelectric MOSFET for low power circuit application with BSIM4 and Landau theory," *Solid State Electron.*, vol. 114, pp. 17–22, Dec. 2015, doi: 10.1016/j.sse.2015.07.001.

[6] H. Ota *et al.*, "Multidomain dynamics of ferroelectric polarization and its coherency-breaking in negative capacitance field-effect transistors," in *IEDM Tech. Dig.*, San Francisco, CA, USA, Dec. 2018, pp. 9.1.1–9.1.4, doi: 10.1109/IEDM.2018.8614531.

[7] K. J. Singh, A. Bulusu, and S. Dasgupta, "Multidomain negative capacitance effect in P(VDF-TrFE) ferroelectric capacitor and passive voltage amplification," *IEEE Trans. Electron Devices*, vol. 67, no. 11, pp. 4696–4700, Nov. 2020, doi: 10.1109/TED.2020.3022745.

[8] A. Rusu and A. M. Ionescu, "Analytical model for predicting subthreshold slope improvement versus negative swing of S-shape polarization in a ferroelectric FET," in *Proc. MIXDES*, Warsaw, Poland, 2012, pp. 55–59.

[9] S. Fujisaki, H. Ishiwara, and Y. Fujisaki, "Low-voltage operation of ferroelectric poly(vinylidene fluoride-trifluoroethylene) copolymer capacitors and metal-ferroelectric-insulator-semiconductor diodes," *Appl. Phys. Lett.*, vol. 90, no. 16, Apr. 2007, Art. no. 162902, doi: 10.1063/1.2723678.

[10] Y. Fujisaki, "Poly(vinylidenefluoride-trifluoroethylene) P(VDF-TrFE)/semiconductor structure ferroelectric-gate FETs," in *Ferroelectric-Gate Field Effect Transistor Memories* (Topics in Applied Physics), vol. 131. Dordrecht, The Netherlands: Springer, 2016, pp. 157–183, doi: 10.1007/978-94-024-0841-6_8.

[11] K. Tashiro and M. Kobayashi, "Structural phase transition in ferroelectric fluorine polymers: X-ray diffraction and infrared/Raman spectroscopic study," *Phase Transitions*, vol. 18, nos. 3–4, pp. 213–246, Aug. 1989, doi: 10.1080/01411598908206864.

[12] *User's Manual for Sentaurus Device*, Synop., Mountain View, CA, USA, 2019.
[13] K. J. Singh, A. Bulusu, and S. Dasgupta, "Origin of negative capacitance transient in ultrascaled multidomain metal-ferroelectric-metal stack and hysteresis-free Landau transistor," *IEEE Trans. Electron Devices*, vol. 69, no. 3, pp. 1284–1292, Mar. 2022, doi: 10.1109/TED.2021.3139057.
[14] R. A. Vega, T. Ando, and T. M. Philip, "Junction design and complementary capacitance matching for NCFET CMOS logic," *IEEE J. Electron Devices Soc.*, vol. 9, pp. 691–703, 2021, doi: 10.1109/JEDS.2021.3095923.
[15] K.-T. Chen *et al.*, "Evaluation of sweep modes for switch response on ferroelectric negative-capacitance FETs," *Appl. Phys. Exp.*, vol. 12, no. 7, Jul. 2019, Art. no. 071003, doi: 10.7567/1882-0786/ab2600.
[16] K. Jang, N. Ueyama, M. Kobayashi, and T. Hiramoto, "Experimental observation and simulation model for transient characteristics of negative-capacitance in ferroelectric $HfZrO_2$ capacitor," *IEEE J. Electron Devices Soc.*, vol. 6, pp. 346–353, Feb. 2018, doi: 10.1109/JEDS.2018.2806920.
[17] B. Obradovic, T. Rakshit, R. Hatcher, J. Kittl, and M. S. Rodder, "Modeling of negative capacitance of ferroelectric capacitors as a non-quasi static effect," 2018, *arXiv:1801.01842*.
[18] P. Sharma, S. Poddar, R. Korlacki, S. Ducharme, and A. Gruverman, "Investigation of ferroelectric domains in thin films of vinylidene fluoride oligomers," *Appl. Phys. Lett.*, vol. 105, no. 2, Jul. 2014, Art. no. 022906, doi: 10.1063/1.4890412.
[19] J. Íñiguez, P. Zubko, I. Luk'yanchuk, and A. Cano, "Ferroelectric negative capacitance," *Nature Rev. Mater.*, vol. 4, no. 4, pp. 243–256, Apr. 2019, doi: 10.1038/s41578-019-0089-0.
[20] A. Stamm, D. J. Kim, H. Lu, C. W. Bark, C. B. Eom, and A. Gruverman, "Polarization relaxation kinetics in ultrathin ferroelectric capacitors," *Appl. Phys. Lett.*, vol. 102, no. 9, Mar. 2013, Art. no. 092901, doi: 10.1063/1.4794865.
[21] S. Khandelwal, J. P. Duarte, A. I. Khan, S. Salahuddin, and C. Hu, "Impact of parasitic capacitance and ferroelectric parameters on negative capacitance FinFET characteristics," *IEEE Electron Device Lett.*, vol. 38, no. 1, pp. 142–144, Jan. 2017, doi: 10.1109/LED.2016.2628349.
[22] M. Mai, B. Martin, and H. Kliem, "Ferroelectric switching in Langmuir–Blodgett and spin-coated thin films of poly(vinylidene fluoride/trifluoroethylene) copolymers," *J. Appl. Phys.*, vol. 110, no. 6, Sep. 2011, Art. no. 064101, doi: 10.1063/1.3636397.
[23] J. Müller *et al.*, "Ferroelectric $Zr_{0.5}Hf_{0.5}O_2$ thin films for nonvolatile memory applications," *Appl. Phys. Lett.*, vol. 99, no. 11, Sep. 2011, Art. no. 112901, doi: 10.1063/1.3636417.
[24] T. Ikegami, K. Fukuda, J. Hattori, H. Asai, and H. Ota, "A TCAD device simulator for exotic materials and its application to a negative-capacitance FET," *J. Comput. Electron.*, vol. 18, no. 2, pp. 534–542, Jun. 2019, doi: 10.1007/s10825-019-01313-7.
[25] S. Horiuchi and Y. Tokura, "Organic ferroelectrics," *Nature Mater.*, vol. 7, no. 5, pp. 357–366, May 2008, doi: 10.1038/nmat2137.
[26] G. A. Salvatore, A. Rusu, and A. M. Ionescu, "Experimental confirmation of temperature dependent negative capacitance in ferroelectric field effect transistor," *Appl. Phys. Lett.*, vol. 100, no. 16, Apr. 2012, Art. no. 163504, doi: 10.1063/1.4704179.
[27] M. Si, X. Lyu, and P. D. Ye, "Ferroelectric polarization switching of hafnium zirconium oxide in a ferroelectric/dielectric stack," *ACS Appl. Electron. Mater.*, vol. 1, no. 5, pp. 745–751, May 2019, doi: 10.1021/acsaelm.9b00092.
[28] P. Sharma, J. Zhang, K. Ni, and S. Datta, "Time-resolved measurement of negative capacitance," *IEEE Electron Device Lett.*, vol. 39, no. 2, pp. 272–275, Feb. 2018, doi: 10.1109/LED.2017.2782261.
[29] K. J. Singh, A. Bulusu, and S. Dasgupta, "Harnessing maximum negative capacitance signature voltage window in P(VDF-TrFE) gate stack," in *Proc. IEEE Int. Symp. Circuits Syst. (ISCAS)*, May 2021, pp. 1–5, doi: 10.1109/ISCAS51556.2021.9401100.
[30] W. Zhao and Y. Cao, "New generation of predictive technology model for sub-45 nm early design exploration," *IEEE Trans. Electron Devices*, vol. 53, no. 11, pp. 2816–2823, Nov. 2006, doi: 10.1109/TED.2006.884077.
[31] *Arizona State University Predictive Technology Models*. Accessed: Oct. 9, 2021. [Online]. Available: http://ptm.asu.edu/
[32] A. K. Saha, P. Sharma, I. Dabo, S. Datta, and S. K. Gupta, "Ferroelectric transistor model based on self-consistent solution of 2D Poisson's, non-equilibrium Green's function and multi-domain Landau Khalatnikov equations," in *IEDM Tech. Dig.*, San Francisco, CA, USA, Dec. 2017, pp. 13.5.1–13.5.4, doi: 10.1109/IEDM.2017.8268385.

KHOIROM JOHNSON SINGH (Graduate Student Member, IEEE) was born in Manipur, India. He received the bachelor's degree in electronics and communication engineering from the National Institute of Technology Manipur, Imphal, India, in 2016, and the master's degree in electronics and communication engineering from the North Eastern Regional Institute of Science and Technology Nirjuli, Arunachal Pradesh, India, in 2018. He is currently pursuing the Ph.D. degree with the Microelectronics and VLSI Group, Department of Electronics and Communication Engineering, Indian Institute of Technology Roorkee, Uttarakhand, India.

His current research interests include ferroelectric devices, capacitors, beyond CMOS transistor technology, and device circuit co-design. He is a member of the IEEE Electron Devices Society (EDS), the IEEE Circuit and Systems Society (CASS), the IEEE Ultrasonics, Ferroelectrics, and Frequency Control Society (UFFC-S), and the International Society for Optics and Photonics (SPIE). He is a recipient of the prestigious INSPIRE Fellowship. He was a recipient of the Institute Gold Medal at the undergraduate and postgraduate levels, respectively. He is a Reviewer in the peer-reviewed journal IEEE TRANSACTIONS ON ULTRASONICS, FERROELECTRICS, AND FREQUENCY CONTROL.

NITANSHU CHAUHAN (Member, IEEE) received the M.Tech. degree in VLSI from the Indian Institute of Technology Roorkee, Uttarakhand, India, in 2017, where he is currently pursuing the Ph.D. degree with the Department of Electronics and Communication Engineering. He is also associated with the Department of Electronics Engineering, NIT Uttarakhand, Srinagar. His current research interests include simulation, modeling of negative capacitance field-effect transistors, FeFET, and device circuit co-design.

ANAND BULUSU (Member, IEEE) received the Ph.D. degree from the Indian Institute of Technology Bombay, Mumbai, India, in 2006. From 2007 to 2008, he worked as a Senior Research Engineer at the Silicon Technology Solutions Groups of Freescale Semiconductor (presently NXP Semiconductor). He is currently working as a Professor with the Department of Electronics and Communication Engineering, Indian Institute of Technology Roorkee, Uttarakhand, India. His current research interests include device physics, circuit performance models and design, device-circuit interaction for emerging and conventional devices, and digital/analog/mixed-signal circuit design.

SUDEB DASGUPTA (Member, IEEE) received the Ph.D. degree in electronics engineering from the Indian Institute of Technology (BHU), Varanasi, in 2000. He is currently working as a Professor and the Head of the Electronics and Communication Engineering Department, Indian Institute of Technology Roorkee, Uttarakhand, India. His research interests include nanoscale MOSFET modeling and simulation, design and development of low-power novel devices, FinFET-based memory design, emerging devices in analog design, design and development of reconfigurable logic, compute-in-memory, and beyond CMOS.